JAAS

ROYAL SOCIETY OF CHEMISTRY

PAPER

View Article Online
View Journal | View Issue

Cite this: *J. Anal. At. Spectrom.*, 2025, **40**, 1505

Depth profiling of noble gases in ilmenite and olivine substrates†

Yuta Otsuki, *[a] Ken-ichi Bajo,[a] Tomoya Obase[ab] and Hisayoshi Yurimoto[a]

Solar wind noble gases in extraterrestrial materials provide important insights into past solar activity and space weathering processes. These noble gases are concentrated within the uppermost 100 nm of material surfaces, requiring *in situ* analysis with high depth and lateral resolution. Additionally, the multi-isotope analysis of noble gases is useful in evaluating the degassing of materials. To address these requirements, we developed a depth profiling method for multi-noble gas isotopes by time-of-flight secondary neutral mass spectrometry. We prepared ilmenite and olivine substrates co-implanted with ^{4}He, ^{20}Ne, ^{22}Ne, ^{36}Ar, and ^{40}Ar as standards for solar wind-irradiated materials and surveyed the optimal analytical conditions to improve the substrate detection limits. As a result, we achieved ^{4}He, ^{20}Ne, ^{22}Ne, ^{36}Ar, and ^{40}Ar detection limits of 7×10^{16}, 3×10^{16}, 9×10^{15}, 2×10^{16}, and 5×10^{16} cm^{-3} for ilmenite and 2×10^{17}, 4×10^{16}, 2×10^{16}, 2×10^{16}, and 9×10^{17} cm^{-3} for olivine, respectively. The reproducibility for the concentration and elemental/isotope ratio measurements ranged from 5% to 31%. This method allowed for the visualization of nano-scale solar wind noble gas distributions on extraterrestrial material surfaces, providing insights into the solar wind activities and space weathering of celestial bodies.

Received 2nd December 2024
Accepted 16th April 2025

DOI: 10.1039/d4ja00430b

rsc.li/jaas

Introduction

Solar wind noble gases in extraterrestrial materials serve as a useful proxy for analyzing solar wind irradiation to reveal past solar activities or space weathering processes.[1,2] The typical energy of a solar wind particle is approximately 1 keV per nucleon, and the implanted particles are concentrated within the top 100 nm of the material surface on airless bodies.[3] Previous studies have anticipated the actual measurements of noble gas profiles in lunar samples,[4] but conventional noble gas mass spectrometers lacked the spatial resolution necessary to reveal the precise distribution of implanted noble gases.

In the 1970s, combining ion beam sputtering and electron ionization, gas ion probes (beam diameter, 200 μm; depth resolution, ~10 nm) were successfully used for the ^{4}He depth profiling of lunar samples.[3,5–8] However, other noble gas isotopes such as ^{20}Ne and ^{36}Ar were difficult to measure in natural samples due to their high background. In addition, all sputtered particles will be ionized from the crater bottom and crater edge, which in principle limits the depth resolution. Recent developments in secondary ion mass spectrometry have led to improvements in the detection limits of the depth profiling of helium and argon implanted into semiconductors and metals in engineering applications. However, the rastering areas of these measurements have been limited to several tens of μm.[9,10] In cosmochemical studies, the depth distribution of noble gases in extraterrestrial materials has been measured by the Closed System Stepwise Etching (CSSE) method, in which a sample is etched stepwise in a vacuum and the noble gases extracted from the sample surface are measured with a noble gas mass spectrometer.[11,12] However, the CSSE method cannot determine the absolute depth of etching.

In recent years, time-of-flight secondary neutral mass spectrometry (TOF-SNMS) has been performed using a laser ionization mass nanoscope (LIMAS).[13–21] The LIMAS uses Ga ion beam sputtering and post-ionization with a femtosecond (fs) laser for high-resolution ^{4}He analysis, reaching a ^{4}He detection limit of 2×10^{17} cm^{-3} with a ~2 μm primary beam spot size.[14] Note that a unit cm^{-3} used here is atoms per cm^{3}, of which unit corresponds to approximately 3.7×10^{-20} ρ^{-1} cm^{3} STP g^{-1}, where ρ is the density (g cm^{-3}) of the host material.

Bajo *et al.*[18] conducted ^{4}He depth profiling in the diamond-like carbon target of NASA/Genesis[22] using a LIMAS to obtain the ^{4}He depth profile. The depth profile was consistent with that of ion implantation simulations performed using the Stopping and Range of Ions in Matter (SRIM) software[23] under the solar wind speed distribution observed by a spacecraft.[24] They proposed that the ^{4}He depth profiling of extraterrestrial materials could reveal the energy distribution of solar wind. Conventional analyses of noble gases in extraterrestrial materials suggest that light noble gases (*i.e.*, He and Ne) are partially

[a]*Department of Natural History Sciences, Faculty of Science, Hokkaido University, Sapporo, Hokkaido 060-0810, Japan. E-mail: yotsuki@ep.sci.hokudai.ac.jp; Tel: +81-11-706-9174*

[b]*Department of Earth and Planetary Sciences, Institute of Science Tokyo, Meguro-ku, Tokyo, 152-8551, Japan*

† Electronic supplementary information (ESI) available. See DOI: https://doi.org/10.1039/d4ja00430b

degassed to a certain degree during or after solar wind irradiation.[1,25,26] Therefore, the simultaneous analysis of Ne and Ar isotopes in addition to ^{4}He to evaluate noble gas retention at each measurement point is of high interest.

In this study, we developed a depth profiling technique for Ne, Ar, and He in minerals. Ilmenite and olivine samples implanted with ^{4}He, ^{20}Ne, ^{22}Ne, ^{36}Ar, and ^{40}Ar were prepared as analogues of solar wind-implanted lunar and asteroidal samples to understand past solar activity using *in situ* depth profiling. In addition to the ^{4}He analysis, we performed the multi-isotope depth profiling of ^{4}He, ^{20}Ne, ^{22}Ne, ^{36}Ar, and ^{40}Ar using LIMAS, achieving low detection limits for the noble gas isotopes.

Materials and methods

Materials for analysis

Ion-implanted substrates were prepared for the noble gases to develop depth profiles of their concentrations and isotopic ratios. Polished substrates of an ilmenite crystal ($(Fe_{0.7}Mg_{0.3})TiO_3$) from Monastery mine, South Africa, and an olivine crystal ($(Mg_{0.9}Fe_{0.1})_2SiO_4$) from San Carlos, USA, were prepared as representative lunar and asteroidal materials for ion implantation. The ion implantations of ^{4}He, ^{20}Ne, ^{22}Ne, ^{36}Ar, and ^{40}Ar were carried out using an ion implanter (ULVAC IMX-3500RS) at the Toray Research Center, Inc. The irradiation energies and doses for each noble gas are summarized in Table 1. Ion implantation was performed at room temperature, and the angle of incidence was set to 0°. Ilmenite and olivine were fixed on a p-type silicon wafer, and ion implantation was carried out simultaneously to produce samples hereafter referred to as HNA-IL and HNA-OL, respectively. The silicon wafer was used for mass assignment because the TOF spectra were much simpler than those of ilmenite and olivine, which was referred to as HNA-Si. The ion implantation doses were certified to ±5% accuracy.

We used polished substrates of Monastery ilmenite and San Carlos olivine without ion implantation, *i.e.*, blank-IL and blank-OL, respectively, to evaluate the backgrounds of the noble gas isotopes. The ilmenite and olivine substrates were coated with ~10 nm of gold before noble gas measurements to reduce electrostatic charge-up due to primary beam irradiation during depth profiling.

Depth profiling by LIMAS

Depth profiling was performed using a JEOL LIMAS[15] at Hokkaido University. A pulsed ^{69}Ga ion beam (30 keV, ~30 nA) was targeted on the sample surface with a focused ion beam system. A primary ion pulse of 400 ns width was focused on a ~2 μm spot and rastered to an area of ~18 × 25 μm^2 (30 × 30 pixels). Sputtered neutral particles were post-ionized using an fs laser (Astrella, Coherent) with an energy of 6 mJ, a pulse width of 35 fs, and a wavelength of 795 nm. Post-ionized ions were injected into a multi-turn TOF mass spectrometer (MULTUM II)[27] with an acceleration voltage of −5 kV. Ions not of interest were removed from the ion trajectory by adjusting the timing of the ion injection and the ion gate in the MULTUM II system. Flight times of several hundred microseconds separated the ions of interest from other interfering ions. The ions of interest were then detected using a high-speed ion detection system using two-stage microchannel plates (MCP; F1217-011, Hamamatsu Photonics). This single sequence from sputtering to ion detection is referred to as a mass scan, and the signal intensity is given in the unit of ion counts per mass scan (cpms). The repetition rate of the mass scan was set to 1 kHz and synchronized with the fs laser system. The timing control and data acquisition systems were based on the description by Bajo *et al.*[16,17]

During depth profiling, 100 mass scans (taking 0.1 s) were collected for one pixel to obtain a TOF spectrum, and all TOF spectra for each pixel were recorded. The rastering of 30 × 30 pixels was repeated for more than several hundred measurement layers (90 s per layer) until the noble gas decreased to a constant intensity, which was considered the background of the noble gas isotope signals. The depth profile was obtained using data from the inner 10 × 10 pixel area to reduce the crater edge effect. After depth profiling, residual gas was measured without primary beam irradiation and referred to as blank ^{i}M (^{i}M: ^{4}He, ^{20}Ne, ^{22}Ne, ^{36}Ar, and ^{40}Ar ions). To compare the backgrounds of the noble gas signals, blank-IL and blank-OL were analyzed under the same analytical conditions as those for HNA-IL and HNA-OL.

After depth profiling, the depth of the sputtering crater was measured using a three-dimensional (3D) confocal laser microscope (VK-X200, Keyence). A typical sputtering crater is shown in Fig. 1. The sputtering rate was calculated by dividing the crater depth by the total number of measurement layers. The precision of the crater depth measurement was ±5% (Fig. S1†).

Table 1 Conditions of ion implantation[a]

Isotope	Energy/keV	Dose/cm^{-2}
^{4}He	20	2.00×10^{15}
^{20}Ne	60	1.00×10^{14}
^{22}Ne	60	1.00×10^{13}
^{36}Ar	110	1.00×10^{13}
^{40}Ar	110	1.00×10^{14}

[a] Implantation experiment was conducted at room temperature.

Calibration for isotope concentrations and isotope ratios of noble gases

Isotope concentrations for noble gas ^{i}M at depth layer k ($C_{^i\mathrm{M},k}$) can be calculated using the relative sensitivity factors (RSFs) as follows:

$$\mathrm{RSF}_{^i\mathrm{M}} = \phi_{^i\mathrm{M}} \times \left(\sum_{k=1}^{n} \left\{ \frac{[^i\mathrm{M}_{\mathrm{std}}]}{[I_{\mathrm{mtx,std}}]}\bigg|_k - \frac{[^i\mathrm{M}_{\mathrm{std}}]}{[I_{\mathrm{mtx,std}}]}\bigg|_{\mathrm{BL}} \right\} \times \frac{d}{n} \right)^{-1}, \quad (1)$$

$$C_{^i\mathrm{M},k} = \mathrm{RSF}_{^i\mathrm{M}} \times \left(\frac{[^i\mathrm{M}_{\mathrm{sam}}]}{[I_{\mathrm{mtx,sam}}]}\bigg|_k - \frac{[^i\mathrm{M}_{\mathrm{sam}}]}{[I_{\mathrm{mtx,sam}}]}\bigg|_{\mathrm{BL}} \right) \quad (2)$$

where $\phi_{^i\mathrm{M}}$ is the ion dose of isotope ^{i}M, while $[^i\mathrm{M}]$ and $[I_{\mathrm{mtx}}]$ are the ion intensities of isotope ^{i}M and matrix isotope for

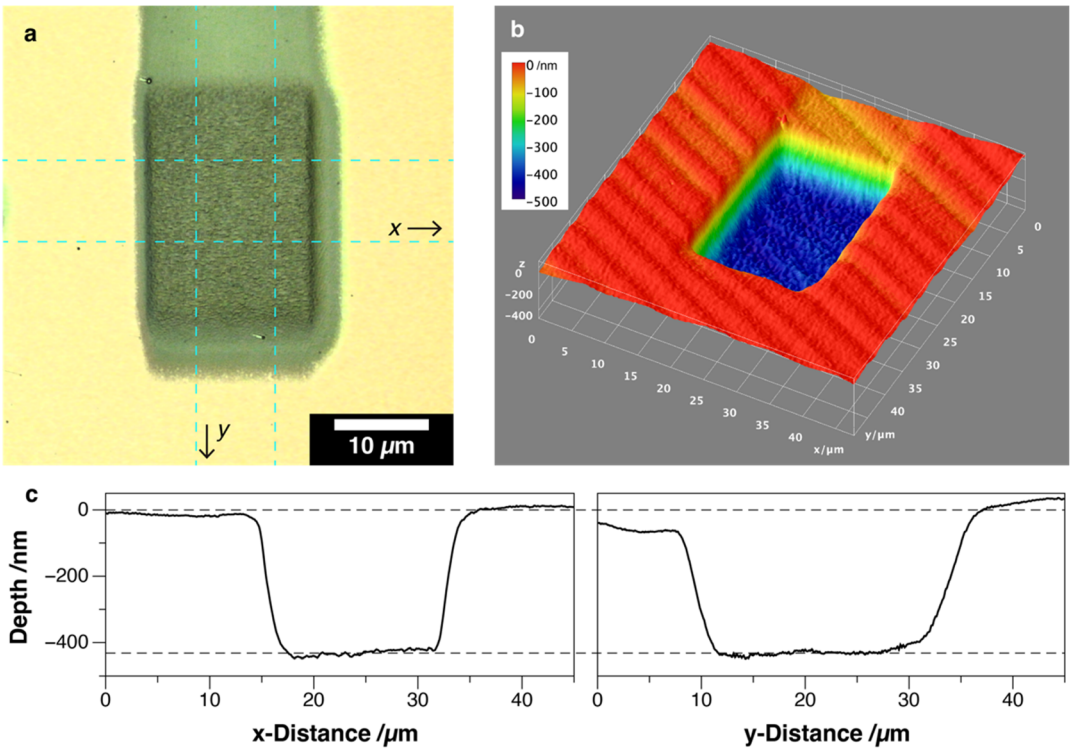

Fig. 1 LIMAS sputter crater on HNA-IL measured using a 3D confocal laser microscope. (a) Laser + RGB image. (b) 3D image. (c) Line profiles obtained in the *x* and *y* directions. The bright area in (a) is coated with gold. The wave on the sample surface in (b) is an artifact from the measurement step of the laser microscope. The line profiles were averaged from the inside of the broken line in (a) for the *x* and *y* directions, so the effect of the wave is negligible. The averaged heights of the sample surface and crater bottom are shown as broken lines in (c), and the depth of this crater was calculated to be 432 nm.

reference, respectively. The std, sam, and BL subscripts denote the standard, unknown sample, and baseline of the depth profile, respectively. d is the depth of the sputter crater and n is the number of measured layers at d. A matrix ion is used here to correct for the gradual changes of ion intensity mainly due to gradual changes of injection efficiency of the MULTUM II, assuming that the ion intensity ratios are correlated with the concentration ratios. The abundance of the matrix ion should be constant in the substrates and the same in the reference and the unknown samples. The ion $^{16}O^{2+}$ was used as a matrix isotope for both HNA-IL and HNA-OL.

The ion intensity ratios of noble gas ions in depth layer k can be converted to elemental or isotopic ratios with RSFs and calculated as follows:

$$\mathrm{RSF}_{i,j} = \frac{\phi_{i\mathrm{M}}}{\phi_{j\mathrm{N}}} \times \left(\frac{\sum_{k=1}^{n} \left\{ [^{i}\mathrm{M}_{\mathrm{std}}]_k - [^{i}\mathrm{M}_{\mathrm{BL,std}}] \right\}}{\sum_{k=1}^{n} \left\{ [^{j}\mathrm{N}_{\mathrm{std}}]_k - [^{j}\mathrm{N}_{\mathrm{BL,std}}] \right\}} \right) \quad (3)$$

$$\left(\frac{^{i}\mathrm{M}}{^{j}\mathrm{N}} \right)_k = \mathrm{RSF}_{i,j} \times \left(\frac{[^{i}\mathrm{M}_{\mathrm{sam}}]_k - [^{i}\mathrm{M}_{\mathrm{BL,sam}}]}{[^{j}\mathrm{N}_{\mathrm{sam}}]_k - [^{j}\mathrm{N}_{\mathrm{BL,sam}}]} \right) \quad (4)$$

Identification of target ion species

To simultaneously measure ^{4}He, ^{20}Ne, ^{22}Ne, ^{36}Ar, ^{40}Ar, and major elements as matrix ions, we optimized the appropriate analytical conditions for mass spectrometry, in which each ion signal of interest was separated from isobaric ions and other signals that can overlap due to overtaking ions with smaller m/z. The TOF T for each ion was calculated using eqn (5):

$$T = L\sqrt{\frac{m/z}{2eV}} + T_{\mathrm{o}} \quad (5)$$

where L is the flight path length, m/z is the mass-to-charge ratio of the ion, e is the elementary charge, V is the acceleration voltage, and T_{o} is the offset time between the trigger signal from the timing controller and the first injection pulse electrode. For the calculation, the flight path length was fixed at 0.910 m from the sample surface to the MCP and 1.317 m for a single lap of the MULTUM II system. Therefore, $L = 0.910 + 1.317N$ (m), where N is the lap number in the MULTUM II system. V is fixed at 5 kV, and T_{o} of the system is ~500 ns.

The values of T for multiple ions were calculated using eqn (5) by adjusting the valence and isotopes to find TOF conditions where all noble gases and major elements of olivine and ilmenite (*i.e.*, O, Mg, Si, Ti, and Fe) did not overlap. The noble gas ions were measured at a shorter TOF than the major element ions, as the tails of the intense peaks interfered with the smaller peaks of the noble gas isotopes. As a result, we found TOF windows for measuring m/z 4 ($^{4}He^{+}$), 8 ($^{16}O^{2+}$), 9 ($^{36}Ar^{4+}$), 10 ($^{20}Ne^{2+}$, $^{30}Si^{3+}$, and $^{40}Ar^{4+}$), 11 ($^{22}Ne^{2+}$), 12 ($^{24}Mg^{2+}$ and $^{48}Ti^{4+}$), and 20 ($^{20}Ne^{+}$ and $^{40}Ar^{2+}$) along with either 18 ($^{36}Ar^{2+}$) or 28 ($^{28}Si^{+}$ and $^{56}Fe^{2+}$) at a TOF of 455–461 μs using the

activation of the ion gate. The calculated TOF spectra of these m/z are shown in Fig. S2.† Under the conditions optimized for measuring other noble gas ions, m/z 18 and 28 overlapped. These ions can be selected by controlling the ion gates of MULTUM II. As we found that using $^{36}Ar^{4+}$ was a better approach as mentioned later, we measured m/z 28 peaks.

In the analysis of natural samples, many other ion peaks from minor and trace elements were detected in addition to the target ions in the TOF spectra. The ion peaks of major elements and implanted noble gases can be first assigned by comparing with calculations and respectively checking the depth profiles, which showed constant intensity during analysis, and peak depth profiles. In addition, the ions of residual gases such as O, N, and Ar can be assigned through blank analysis. The exact m/z values of unknown peaks, such as minor and trace element ions, can be calculated from the TOF difference ΔT between the unknown and the known ion peak if the lap number is the same. The following equation was used for the calculations:

$$m/z = \left(\sqrt{(m/z)_{\text{known}}} - \Delta T \times \frac{\sqrt{2eV}}{L}\right)^2 \quad (6)$$

Ion implantation simulation

We simulated the depth profile of the noble gases in the substrates using the Transport of Ions in Matter (TRIM) in the SRIM program.[23] The simulation parameters for ilmenite and olivine are $(Fe_{0.7}Mg_{0.3})TiO_3$ and $(Mg_{0.9}Fe_{0.1})_2SiO_4$ for stoichiometry and 4.47 and 3.35 g cm^{-3} for density, respectively. The implantation energy was set as the same as that of HNA-IL and HNA-OL as listed in Table 1. The numbers of simulated ions were 10^6 for ^{4}He and ^{20}Ne, 5×10^5 for ^{40}Ar, and 10^5 for ^{22}Ne and ^{36}Ar, respectively. The depth profiles were binned in 5 nm bins and calculated for the doses (Table 1) of each noble gas (Fig. S3†).

Results and discussion

Time-of-flight spectra of standard samples

Fig. 2a shows the TOF spectrum obtained from HNA-Si. The full width at half maximum (FWHM) of the peak at 455.656 μs (assigned later as $^4He^+$) was 9 ns, where $m/\Delta m$ is ~25 000. We defined the ion intensity by integrating the ion at ±9 ns from the peak TOF, which covered 99.05% of the peak at 455.656 μs. This range was set based on the FWHM of the peak for each analysis.

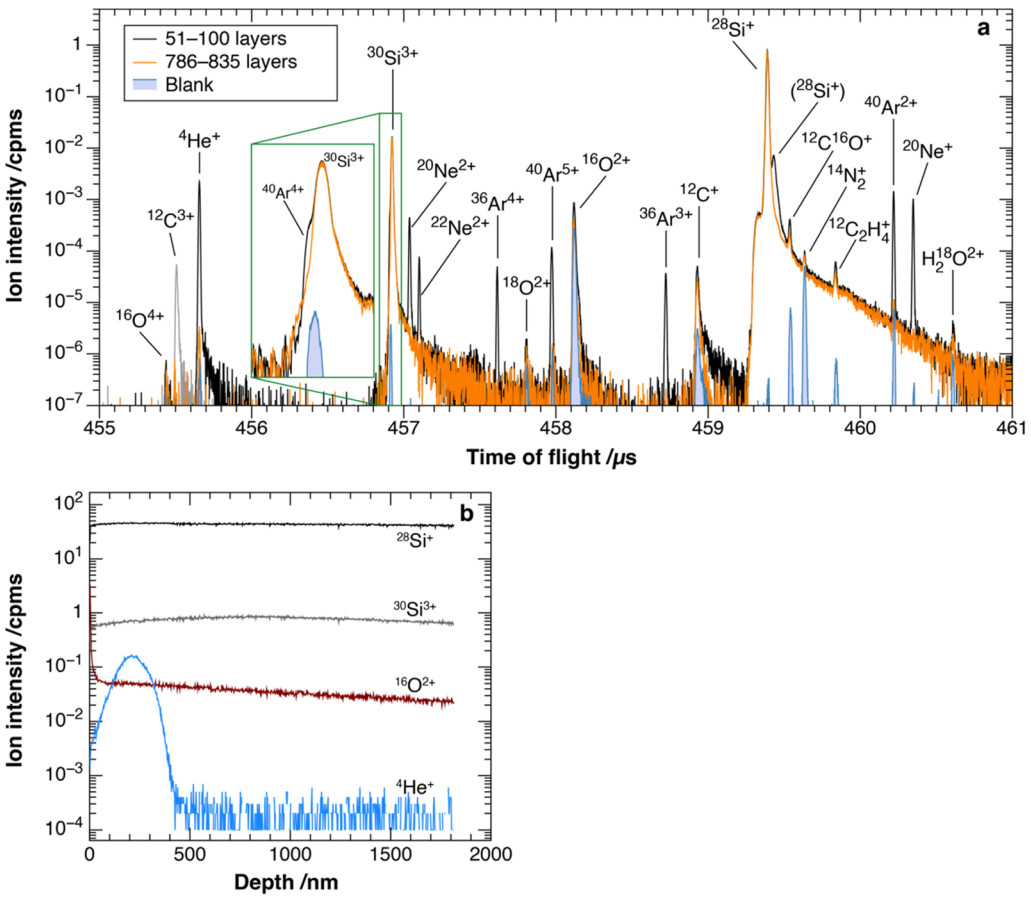

Fig. 2 (a) TOF spectra and (b) depth profile of $^{28}Si^+$, $^{30}Si^{3+}$, $^{16}O^{2+}$, and $^4He^+$ obtained from HNA-Si. Black, orange, and blue lines in (a) are the respective spectra obtained from the depth of the noble gas peak (51–100 layers, 110–217 nm), the last 50 layers in the measurement (786–835 layers, 1708–1814 nm), and the blank signal. The gray line drawn in the range of 455–456 μs is a spectrum recorded after 835 layers without removing the $^{12}C^{3+}$ peak with an ion gate. The TOF spectra of 786–835 layers and the blank signal used a slight offset (~10 ns) to correct for TOF drift during analysis.

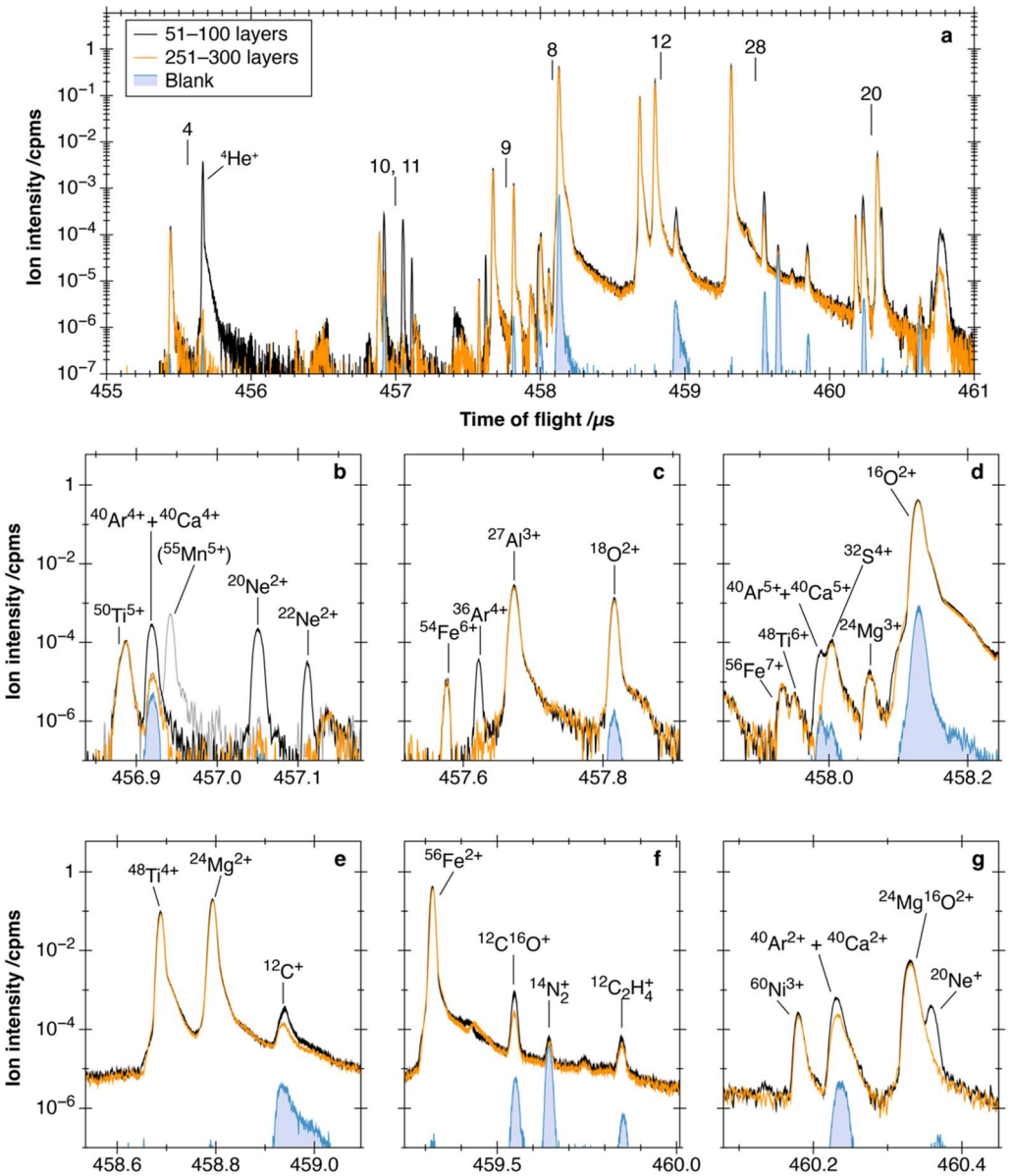

Fig. 3 (a) TOF spectra of HNA-IL; (b)–(g) magnified spectra of (a). Each color corresponds to the noble gas peak, the last part of the analysis, and the blank signal after analysis. The $^{55}Mn^{5+}$ peak shown by the gray line in (b) was recorded after 300 cycles and was removed using the ion gate, as the peak interfered with the $^{40}Ar^{4+}$ and $^{40}Ca^{4+}$ peaks.

The peak assignments were applied by the procedure described in the *Identification of target ion species* section (Fig. 2a). The two high-intensity peaks at 456.923 and 459.389 μs remained constant throughout the analysis (Fig. 2b) and were respectively assigned to $^{30}Si^{3+}$ and $^{28}Si^+$. A long tail was observed after the $^{30}Si^{3+}$ and $^{28}Si^+$ peaks, which was a signal in the MCP induced by a large number of ions striking the channels of MCP (hereafter referred to as dark currents).[15] The peak profile of $^4He^+$, $^{20}Ne^{2+}$, $^{22}Ne^{2+}$, $^{36}Ar^{4+}$, $^{40}Ar^{5+}$, $^{36}Ar^{3+}$, $^{40}Ar^{2+}$, and $^{20}Ne^+$ derived from ion implantations is shown in Fig. 2a. The peak at 458.119 μs representing adsorbed $^{16}O^{2+}$ was intense at the beginning of the depth profile and decreased rapidly (Fig. 2b). Five peaks were observed in the TOF window of m/z 28. Based on the TOF of the $^{28}Si^+$ peak (459.389 μs) and eqn (6), the peaks at 459.537, 459.633, and 459.839 μs were assigned as $^{12}C^{16}O^+$, $^{14}N_2^+$, and $^{12}C_2H_4^+$, respectively (Fig. 2a). The peak at 459.432 μs was assigned to the secondary ion of ^{28}Si because this peak was also detected with the primary beam on and without the fs laser. The $^{12}C^{3+}$ peak, which interfered with the $^4He^+$ peak, was removed using the ion gate in the ion trajectory (Fig. 2a). The peaks of the target ions from the HNA-IL and HNA-OL samples were assigned using the same assignment procedure (Fig. 3 and 4).

For HNA-IL, $^4He^+$ did not show interference from other peaks (Fig. 3a). The right-hand side slope of the $^{24}Mg^{16}O^{2+}$ peak overlapped with the $^{20}Ne^+$ peak (Fig. 3g). $^{20}Ne^{2+}$ was not interfered with by other ion peaks, while $^{22}Ne^{2+}$ was not fully resolved from an unknown peak (Fig. 3b). $^{36}Ar^{4+}$ was interfered with by the left-hand side slope of the $^{27}Al^{3+}$ peak (Fig. 3c).

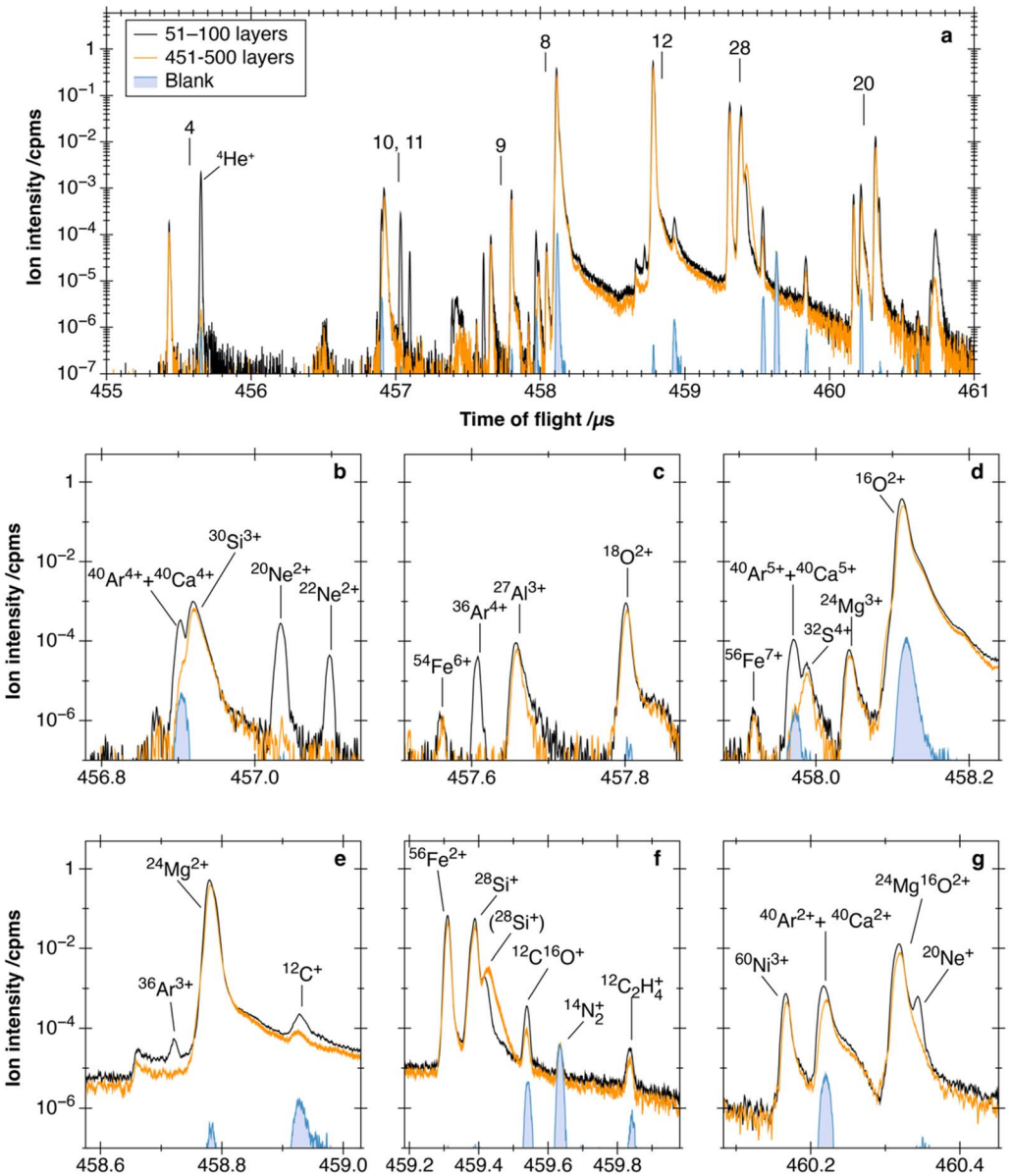

Fig. 4 (a) TOF spectra of HNA-OL; (b)–(g) magnified spectra of (a). Each color corresponds to the noble gas peak, the last part of the analysis, and the blank signal after analysis. ($^{28}Si^+$) in (f) is the secondary ion peak of ^{28}Si.

However, it was less interfered with by other peaks, as $^{36}Ar^{2+}$ and $^{36}Ar^{3+}$ were not fully resolved from $^{54}Fe^{3+}$ and ($^{24}Mg^{2+}$ + $^{48}Ti^{4+}$), respectively (Fig. S4† and potentially seen in Fig. 3e but not observed). The TOF spectra of $^{40}Ar^{2+}$, $^{40}Ar^{4+}$, and $^{40}Ar^{5+}$ showed overlap by ^{40}Ca ions due to the insufficient mass resolution of the analytical conditions (Fig. 3b, d and g). The mass resolution using the FWHM of the $^{40}Ar^{2+}$ peak in the HNA-Si spectrum was ~27 000 (Fig. 2a), but the $m/\Delta m$ of ^{40}Ar and ^{40}Ca was 190 000. We mainly used $^{40}Ar^{4+}$ to match the valence with $^{36}Ar^{4+}$ and also analyzed $^{40}Ar^{2+}$ for comparison. The $^{55}Mn^{5+}$ peak was located at 456.940 μs between the $^{40}Ar^{4+}$ and $^{20}Ne^{2+}$ peaks (Fig. 3b). The $^{55}Mn^{5+}$ peak was removed using the ion gate during noble gas measurements. Ion gate operation did not affect the $^{40}Ar^{4+}$ peak, as it was operated when the ion packets at m/z 10 and 11 were well separated before the TOF of 456.9 μs.

For HNA-OL, $^4He^+$ did not show interference from other peaks (Fig. 4a). $^{20}Ne^+$ had interference from the $^{24}Mg^{16}O^{2+}$ peak for the same reason as that for the HNA-IL measurement (Fig. 4g). The tail from the $^{30}Si^{3+}$ peak, produced by the dark currents, slightly overlapped with both $^{20}Ne^{2+}$ and $^{22}Ne^{2+}$ peaks (Fig. 4b). $^{36}Ar^{4+}$ did not show interference from other peaks (Fig. 4c). Fig. 4g, b and d show the TOF spectra of $^{40}Ar^{2+}$, $^{40}Ar^{4+}$, and $^{40}Ar^{5+}$, respectively, where ^{40}Ca ions overlap with ^{40}Ar ions similar to that in the HNA-IL measurements.

Depth profile of noble gases in minerals

Blank-IL and blank-OL were measured under the same analytical conditions and the depth profiles are shown in Fig. S5.† The backgrounds of noble gas ions for blank-IL and blank-OL are listed in Table 2 with blank ^{i}Ms (ion intensities of each residual

Table 2 Background and blank ^{i}M of noble gas implanted and non-implanted substrates[a]

	$^{4}He^{+}$	$^{20}Ne^{2+}$	$^{22}Ne^{2+}$	$^{36}Ar^{4+}$	$^{40}Ar^{4+}$
Blank-IL	$(4.6 \pm 1.2) \times 10^{-5}$	$(8.0 \pm 11.5) \times 10^{-6}$	$(2.0 \pm 2.7) \times 10^{-6}$	$(2.6 \pm 1.2) \times 10^{-5}$	$(1.0 \pm 0.1) \times 10^{-3}$
Blank ^{i}M	$(3.9 \pm 1.8) \times 10^{-5}$	$(5.0 \pm 5.0) \times 10^{-6}$	$(1.0 \pm 2.2) \times 10^{-6}$	$(1.0 \pm 2.2) \times 10^{-6}$	$(3.2 \pm 0.5) \times 10^{-4}$
Blank-OL	$(9.6 \pm 1.7) \times 10^{-5}$	$(5.6 \pm 1.6) \times 10^{-5}$	$(2.3 \pm 1.2) \times 10^{-5}$	$(4.0 \pm 6.5) \times 10^{-6}$	$(2.8 \pm 0.2) \times 10^{-3}$
Blank ^{i}M	$(4.9 \pm 1.0) \times 10^{-5}$	$(9.0 \pm 8.2) \times 10^{-6}$	$(1.0 \pm 2.2) \times 10^{-6}$	$(1.0 \pm 2.2) \times 10^{-6}$	$(4.5 \pm 0.4) \times 10^{-4}$
HNA-IL	$(1.1 \pm 0.1) \times 10^{-4}$	$(2.9 \pm 1.6) \times 10^{-5}$	$(5.0 \pm 6.1) \times 10^{-6}$	$(4.6 \pm 1.0) \times 10^{-5}$	$(6.6 \pm 0.4) \times 10^{-4}$
Blank ^{i}M	$(1.6 \pm 0.8) \times 10^{-5}$	$(6.0 \pm 5.5) \times 10^{-6}$	$(1.0 \pm 2.2) \times 10^{-6}$	n.d.	$(1.5 \pm 0.2) \times 10^{-4}$
HNA-OL	$(1.1 \pm 0.3) \times 10^{-4}$	$(3.1 \pm 0.7) \times 10^{-5}$	$(4.0 \pm 4.2) \times 10^{-6}$	$(6.0 \pm 4.2) \times 10^{-6}$	$(8.1 \pm 0.3) \times 10^{-3}$
Blank ^{i}M	$(3.0 \pm 1.0) \times 10^{-5}$	$(5.0 \pm 5.0) \times 10^{-6}$	n.d.	n.d.	$(1.4 \pm 0.2) \times 10^{-4}$

[a] Units are cpms. n.d.: not detected ($<10^{-6}$ cpms).

noble gas in the sample chamber) measured continuously throughout each analysis. The noble gas background was defined as the average of 10^6 mass scans after sputtering to ~100 nm depth to avoid contamination on the sample surface. The error was defined as the standard deviation (1SD) of five data points obtained by binning the data into 2×10^5 mass scans. Similarly, blank ^{i}M was defined as the average of 10^6 mass scans, with the error determined as the 1SD of five data points by binning into 2×10^5 mass scans.

The blank-IL and blank-OL backgrounds were in agreement with the blank ^{i}Ms within the standard deviation (Table 2) for ions with less interference from other peaks (*i.e.*, $^{4}He^{+}$, $^{20}Ne^{2+}$, and $^{22}Ne^{2+}$ for blank-IL and $^{36}Ar^{4+}$ for blank-OL). Therefore, the influence of noble gases originally contained in the minerals was smaller than that of residual gases in the sample chamber. For $^{4}He^{+}$ in blank-OL, the background was twice as high as that in blank $^{4}He^{+}$. Similar results were observed by Bajo *et al.*,[14] who mentioned the possible sputtering of ^{4}He adsorbed onto the sputtered surface from residual gas in the sample chamber. Therefore, the degree of adsorption may vary between materials. For other ions, the higher backgrounds for blank-OL and blank-IL compared with blank ^{i}Ms were due to the interference mentioned in the previous section.

The depth profiles of noble gases and selected major ions of HNA-IL and HNA-OL are shown in Fig. 5 and 6. For both samples, all noble gas ions showed a peak at a depth of several tens to ~100 nm, which decreased to a background intensity deeper than 300 nm. The measured depth profiles were slightly distributed at shallower depths than the simulated profiles (Fig. S3†), which are broadly consistent by considering some electrostatic charge-up of the substrates during ion implantation experiments. The background is defined as the average of the last 10^6 mass scans for each noble gas isotope (Fig. 5a and 6a). We evaluated the error of the background by binning these data into 5 data points and calculating the standard deviation (2×10^5 mass scans per point). The backgrounds and blank ^{i}Ms are summarized in Table 2.

The backgrounds of $^{4}He^{+}$ for HNA-IL and HNA-OL were higher than those of blank-IL and blank-OL, respectively (Table 2), which may be ascribed to the crater-edge effect. The image of $^{4}He^{+}$ accumulated for the last 100 layers of HNA-IL is shown in Fig. 7a. The $^{4}He^{+}$ intensity of the outer few pixels was significantly higher than that of the central area, broadening the depth profile shown in Fig. 7b from the crater-edge effect. The averaged intensity of the last 100 layers with changing data integration area is shown in Fig. 7c. The intensity was nearly constant after removing the outer 7 pixels. The depth profiles shown in Fig. 5 removed the outer 10 pixels, sufficiently reducing the crater-edge effect. The higher backgrounds than those of blank-IL and blank-OL may have been caused by the weak halo of the primary beam. Nagata *et al.*[19] reported that a very weak halo spreads out from the center of the primary beam in the LIMAS. The weak halo consistently sputtered the high-concentration layer exposed on the crater edge, interfering with the signals from the crater bottom. We refer to this phenomenon as the weak halo effect. Both $^{4}He^{+}$ and $^{20}Ne^{2+}$ in HNA-IL and HNA-OL exhibited background intensities approximately three orders of magnitude lower than their peak intensities (Fig. 5a and 6a), supporting the idea of a common cause for the higher background.

The backgrounds of other ions of HNA-IL and HNA-OL were similar to those of blank-IL and blank-OL due to the respective interfering ions. The backgrounds of $^{20}Ne^{2+}$ and $^{40}Ar^{4+}$ were respectively lower than those of $^{20}Ne^{+}$ and $^{40}Ar^{2+}$. The $^{20}Ne^{+}$ peak showed interference from the $^{24}Mg^{16}O^{2+}$ peak. However, the interference of $^{24}Mg^{16}O^{4+}$ with $^{20}Ne^{2+}$ was not detected. $^{40}Ca^{4+}$ was much less ionized than $^{40}Ca^{2+}$. Thus, we used $^{20}Ne^{2+}$ and $^{40}Ar^{4+}$ peaks for the ^{20}Ne and ^{40}Ar measurements, respectively.

Detection limits of noble gases

The ion intensity profiles of HNA-IL and HNA-OL were normalized with the $^{16}O^{2+}$ profile to calculate $RSF_{^{i}M}$ using eqn (1) (Fig. 5b and 6b). The baseline was calculated using the last 10^6 mass scans. We subtracted the baseline from the relative intensity and calculated the concentration profile using eqn (2) (Fig. 5c and 6c). We defined the detection limits by multiplying $RSF_{^{i}M}$ by 3SD of the baseline. The standard deviation was calculated by binning the last 10^6 mass scans within 2×10^5 mass scans. The detection limits for each noble gas ranged from 9×10^{15} to 9×10^{17} cm^{-3} depending on each interference and

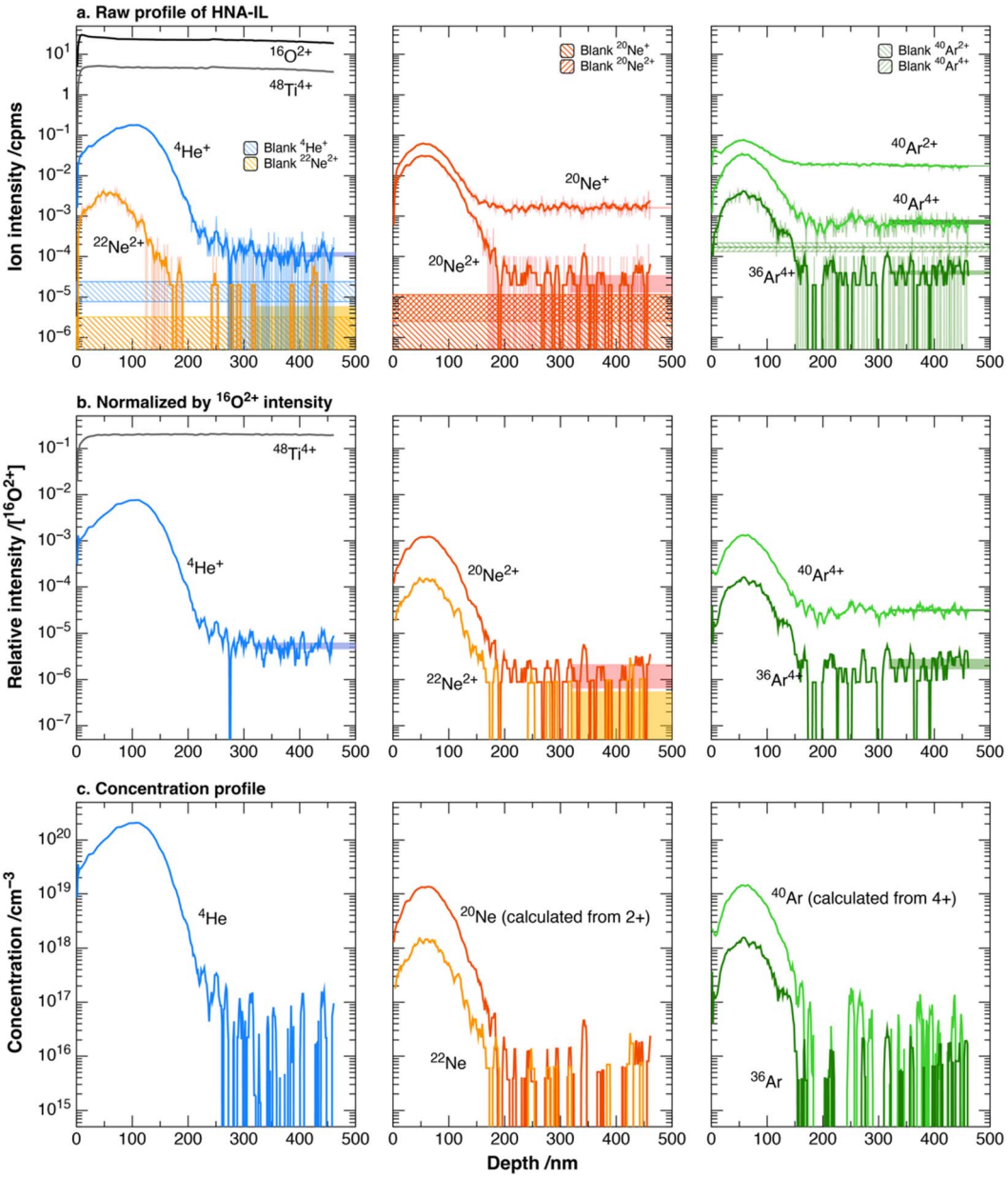

Fig. 5 Noble gas depth profiles of HNA-IL. (a) Raw profile of the noble gas and major element ions (Table S1†). The raw data are shown as a light-colored line with the moving average as a dark solid line. The moving average was calculated over an interval of 5 data points. Blank *i*Ms and backgrounds for each ion are shown as a colored range corresponding with the average ± 1SD (Table 2). (b) Ion intensities normalized by the $^{16}O^{2+}$ intensity. The moving average with an interval of 5 data points is shown. $^{20}Ne^{+}$ and $^{40}Ar^{2+}$ were omitted to simplify the figure. The colored range is the baseline with 1SD for each ion. The mean value was calculated using the last 10^{6} mass scans, and the standard deviation was calculated by binning data points into 5 points, the same as that for the backgrounds. (c) The baseline was subtracted from the normalized profile corrected to concentration using eqn (1) and (2). The moving average with an interval of 5 data points is shown.

standard deviation of base lines. Detection limits of all noble gases are summarized in Table 3. The detection limit of ^{40}Ar was different between two samples. This is due to the differences in calcium abundance in Monastery ilmenite and San Carlos olivine. In addition, detection limits of ^{4}He and ^{22}Ne also differed between the two samples, which could be due to slight differences in the weak halo effect.

Solar wind noble gases are concentrated on the very surface of extraterrestrial materials. Based on the single-grain analyses of lunar ilmenites,[28] the concentrations of ^{4}He, ^{20}Ne, ^{22}Ne, and ^{36}Ar were estimated to be approximately 10^{21}, 10^{19}, 10^{18}, and 10^{18} cm^{-3}, respectively, assuming that all noble gases were concentrated to the top 100 nm of the spherical grain. The detection limits we achieved were approximately more than two orders of magnitude lower than the concentrations in lunar soils, allowing for the depth profiling of ^{4}He, ^{20}Ne, ^{22}Ne, and ^{36}Ar from the grain surface with extremely high spatial resolution.

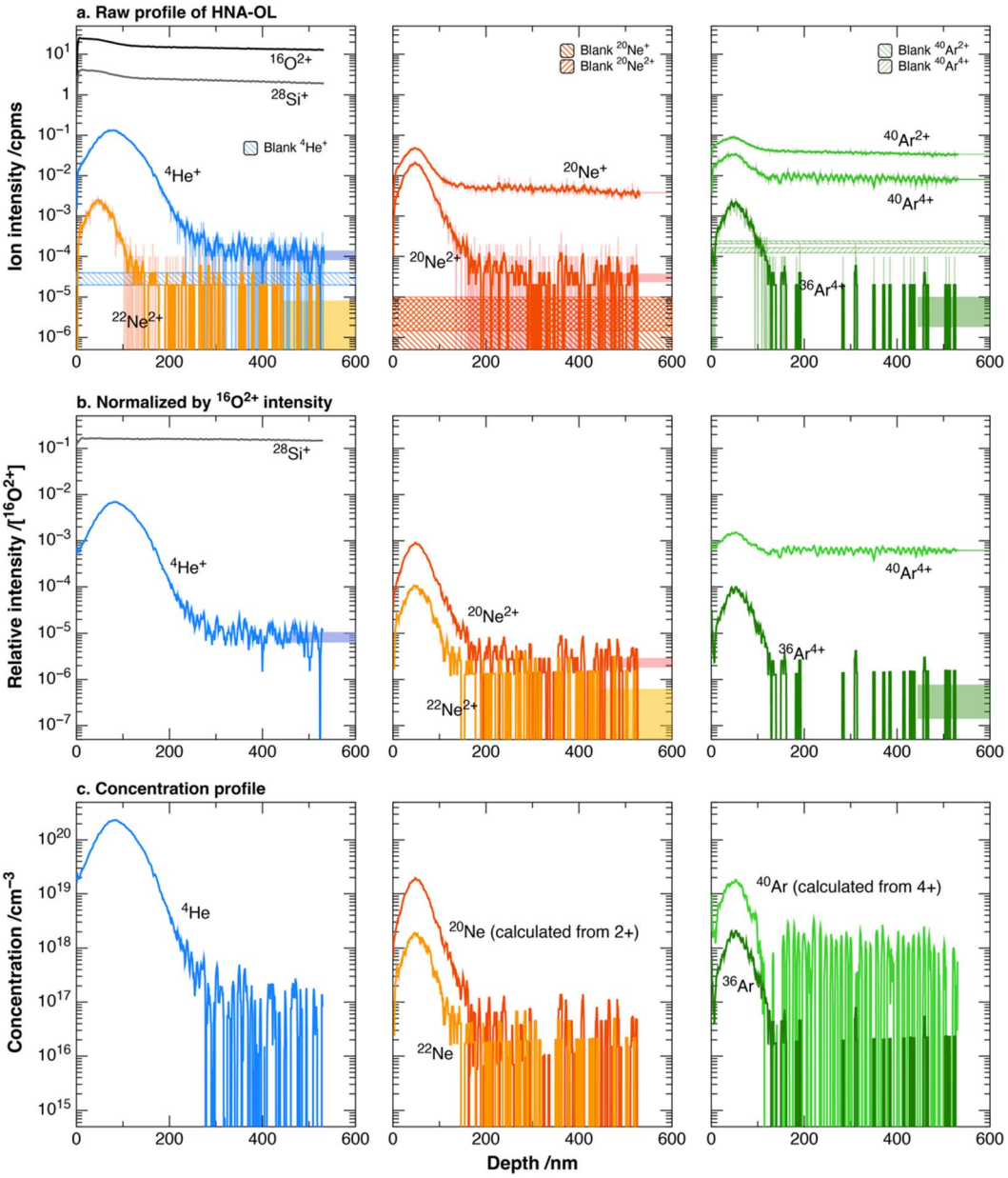

Fig. 6 Noble gas depth profiles of HNA-OL. (a) Raw profile of noble gas and major element ions (Table S2†). The three graphs were obtained in a single measurement but separated to simplify the figure. The raw data are shown as a light-colored line with the moving average as a dark solid line. The moving average was calculated over an interval of 5 data points. Blank ^{i}Ms and backgrounds for each ion are shown as a colored range corresponding to the average ± 1SD (Table 2). (b) Ion intensities normalized by $^{16}O^{2+}$ intensity. The moving average with an interval of 5 data points is shown. $^{20}Ne^{+}$ and $^{40}Ar^{2+}$ were omitted to simplify the figure. The colored range is the baseline with 1SD for each ion. The mean value was calculated using the last 10^{6} mass scans, and the standard deviation was calculated by binning data points into 5 points, the same as that for the backgrounds. (c) Baseline-subtracted normalized profile corrected for concentration using eqn (1) and (2). The moving average with an interval of 5 data points is shown.

Reproducibility of noble gas analysis by LIMAS

We conducted eleven measurements on HNA-IL to calculate the RSFs for concentrations of each noble gas isotope and at selected elemental and isotopic ratios (Fig. 8 and Table S3†). Each measurement run took about 12 h, and the eleven measurements were conducted over a period of 6 months. The standard deviations by counting statistics for each run were less than 5%. The reproducibility of RSFs including $RSF_{i,j}$ and $RSF_{^{i}M}$ showed a variation of 11–31%, which was much larger than the statistical errors (Fig. 8).

The instrumental mass fractionation in the LIMAS arises primarily from two factors: (a) change of laser post-ionization efficiency due to the differences in ionization efficiencies between isotopes or between elements and between independent measurements and (b) the differences in ion transmittance into MULTUM II and within MULTUM II between different lap

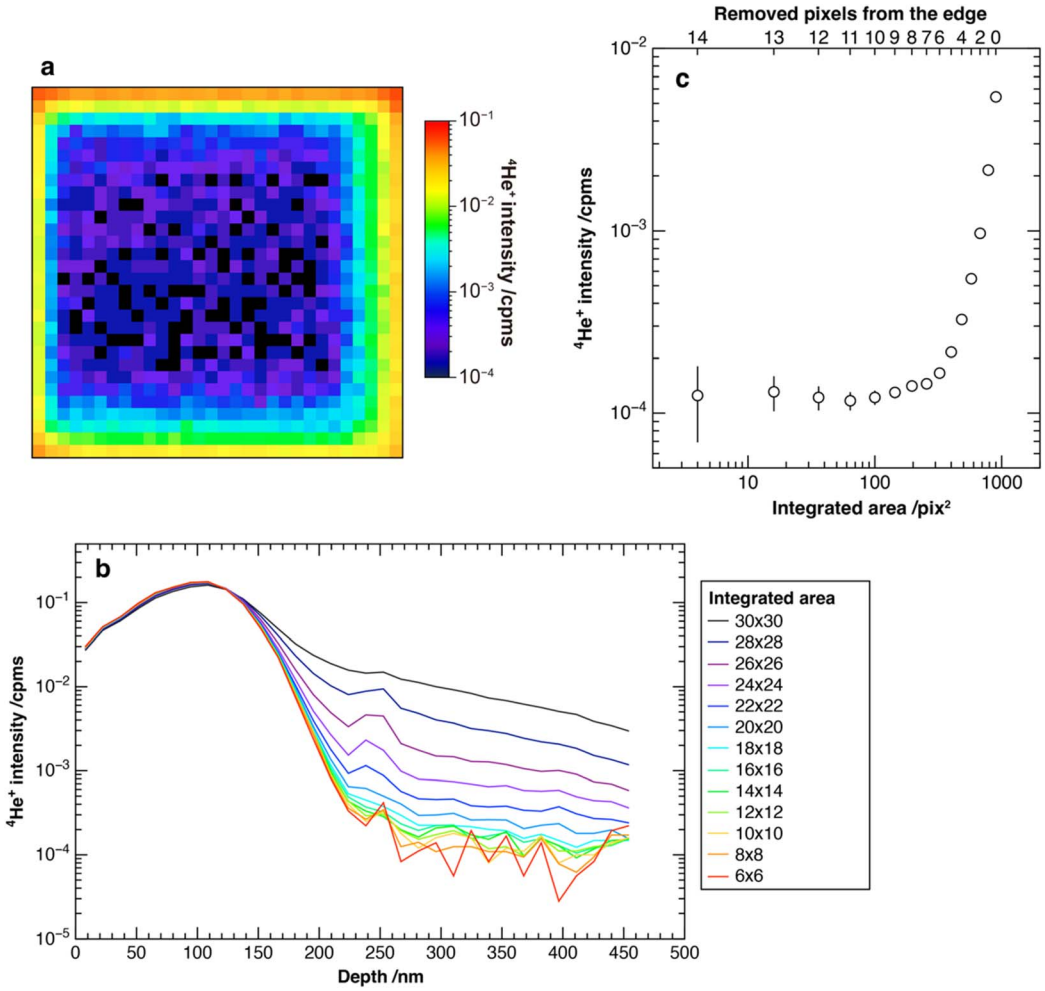

Fig. 7 (a) $^4He^+$ image accumulated for the last 100 layers of HNA-IL, (b) depth profile binned within 10 measurement layers with changing integration area, and (c) averaged $^4He^+$ intensity of the last 50 measurement layers *versus* the integration area from the center. The outer 7 pixels were significantly affected by the crater edge, so the shapes of the profiles from the large integrated areas were worse than those from the smaller areas.

numbers[20] for ions and between independent measurements. $^{20}Ne^{2+}$ and $^{40}Ar^{4+}$ are both measured after 107 laps in the MULTUM II, and thus, $RSF_{20,40}$ is only affected by factor (a). Its standard deviation is 5%, which is the highest reproducibility, and this indicates that relative ionization efficiencies between Ne^{2+} and Ar^{4+} were stable. On the other hand, $RSF_{20,22}$ is affected solely by factor (b) because isotopes would have similar ionization efficiency to each other, and the standard deviation was 12%. This is due to the change of relative ion transmittance between ions with 102–107 laps in the MULTUM II between independent measurements. The standard deviations of $RSF_{20,36}$ and $RSF_{4,20}$ are 11% and 31%, respectively. The former

Table 3 Detection limits (3SD criteria) and major limiting factors for noble gases implanted in olivine and ilmenite[a]

	HNA-IL			HNA-OL		
Isotopes	Measured ions	Detection limits/cm^{-3}	Major interference	Measured ions	Detection limits/cm^{-3}	Major interference
^{4}He	$^4He^+$	7×10^{16}	WHE or residual gas	$^4He^+$	2×10^{17}	WHE or residual gas
^{20}Ne	$^{20}Ne^{2+}$	3×10^{16}	WHE or residual gas	$^{20}Ne^{2+}$	4×10^{16}	$^{30}Si^{3+}$ tail
^{22}Ne	$^{22}Ne^{2+}$	9×10^{15}	WHE or residual gas	$^{22}Ne^{2+}$	2×10^{16}	$^{30}Si^{3+}$ tail
^{36}Ar	$^{36}Ar^{4+}$	2×10^{16}	$^{27}Al^{3+}$ + residual gas	$^{36}Ar^{4+}$	2×10^{16}	WHE or residual gas
^{40}Ar	$^{40}Ar^{4+}$	5×10^{16}	$^{40}Ca^{4+}$ + residual gas	$^{40}Ar^{4+}$	9×10^{17}	$^{40}Ca^{4+}$ + $^{30}Si^{3+}$

[a] WHE: weak halo effect

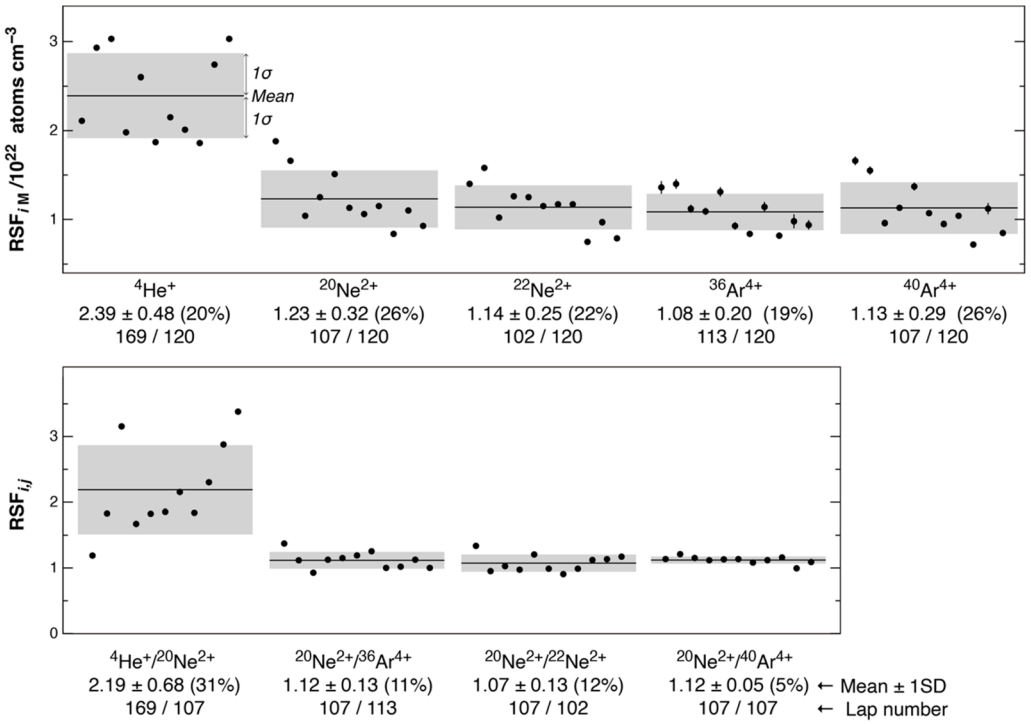

Fig. 8 Reproducibility of RSFs in 11 HNA-IL measurements. Error bars denote the counting errors in 1SD, with most being smaller than the symbol. The mean values and 1SD are described for each RSFs and shown as solid lines and gray regions, respectively. The numbers noted below the mean values are lap numbers of each ion in MULTUM II. Data are listed in Table S3.†

reflects the propagation of the reproducibility of factors (a) and (b), with factor (b) being the dominant contributor. The latter shows the worst reproducibility because the flight path length of $^{4}He^{+}$ is ∼1.5 times longer than those of Ne and Ar ions measured here, and this would be more sensitive to factor (b). In addition, ionization efficiency of He^{+} may also vary relative to Ne^{2+} and Ar^{4+} because of the extremely high ionization energy. The standard deviations of $RSF_{i,M}$ are in the range of 19–26% (1SD). Both factors (a) and (b) affect here. In addition, the calculation of the $RSF_{i,M}$ uses the sputtering rate (d/n in eqn (1)), which includes the measurement errors of the laser microscope of ∼5% (Fig. S1†).

Fig. 9 shows the simulated and measured $^{20}Ne/^{22}Ne$ depth profiles. The simulation suggests that the $^{20}Ne/^{22}Ne$ ratio of HNA-IL in the 0–100 nm range was maintained at 10. We binned the measured ^{20}Ne and ^{22}Ne data to make the counting error for $^{20}Ne/^{22}Ne$ less than 10%. As a result, 13 data points were obtained within the 0–100 nm range. The mean value of these 13 points was 10.1 ± 0.9 (1SD), with 1SD comparable to the counting error of each data point. This indicated that the isotope ratios during the single depth profiling were sufficiently uniform within the error. The ratio could be measured at a depth resolution of ∼10 nm with a precision of 10%.

The single-grain analyses of lunar ilmenites showed that the concentrations of ^{4}He, ^{20}Ne, and ^{36}Ar varied by two to three orders of magnitude among individual grains.[28] Consequently, the reproducibility of $RSF_{i,M}$ (∼20% for all isotopes) was sufficient for the concentration analysis. $^{4}He/^{20}Ne$ and $^{20}Ne/^{36}Ar$ ratios provide insights into the degassing of light noble gases from lunar soils. The single-grain analyses of lunar ilmenites revealed $^{4}He/^{20}Ne$ and $^{20}Ne/^{36}Ar$ ratios of 34–495 and 6–40, respectively, which are minimum and maximum values of ilmenite grains separated from lunar soil 71 501 reported by Nichols *et al.* (1994).[28] Thus, the reproducibility of $RSF_{4,20}$ and $RSF_{20,36}$ (31% and 11%) was sufficient to estimate the bulk $^{4}He/^{20}Ne$ and $^{20}Ne/^{36}Ar$ ratios in lunar ilmenites. The $^{20}Ne/^{22}Ne$

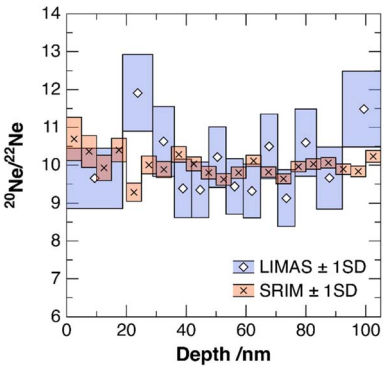

Fig. 9 $^{20}Ne/^{22}Ne$ ratio with depth for HNA-IL and SRIM. LIMAS data were binned to make the counting error less than ±10%, shown as the blue range. The SRIM depth profile calculated within a 5 nm bin is shown with the counting error in 1SD. $^{20}Ne/^{22}Ne$ in the <100 nm region was nearly constant at 10. The relative standard deviation of 13 plots measured using the LIMAS was 9%, indicating that the counting error constrained the uncertainty for each data point in depth.

ratio of materials irradiated by solar wind indicated depth-dependent mass fractionation during solar wind implantation.[11] Closed system stepwise etching indicated that the $^{20}Ne/^{22}Ne$ ratio of lunar ilmenite was ~14 at the surface and ~11 in the subsurface region.[12] The reproducibility of $RSF_{20,22}$ (~12%) and the $^{20}Ne/^{22}Ne$ depth profile obtained using the LIMAS suggested that the fractionation of Ne isotopes could be visualized with actual depth, allowing for the more precise characterization of the implantation profile of solar wind noble gases.

Applicability to other extraterrestrial samples

This study demonstrates a measurement technique optimized for ilmenite and olivine, because we focus on measurements of lunar and asteroidal regolith samples. The results indicate that one critical factor for the optimization is to consider the sample composition, which influences detection limits due to interfering ions. For example, in materials with higher aluminum or silicon content, interferents such as $^{27}Al^{3+}$ to $^{36}Ar^{4+}$ or $^{30}Si^{3+}$ and $^{40}Ca^{4+}$ overlapping with $^{20}Ne^{2+}$ and $^{40}Ar^{4+}$ may become significant. In such cases, the TOF conditions and selected ions to be measured optimized in this study may not be ideal, necessitating modifications to measurement parameters according to the discussion in this study. Preparation of ion-implanted reference samples is also necessary in such cases.

A possible application of this method is for noble gases trapped in presolar grains or interplanetary dust particles, whose sample sizes are much smaller than typical lunar or asteroidal sample sizes. To ensure high depth resolution for the depth profiling, a large smooth surface relative to the primary beam diameter is required. Therefore, a smaller primary beam diameter is needed. In order to achieve it, the primary beam current must be reduced. However, reducing the beam current leads to lower ion intensities per mass scan, which, in turn, raises the detection limit for noble gases.

Despite these challenges, the method presented here represents a novel approach to obtaining depth profiles of He, Ne, and Ar isotopes and their compositions based on an absolute depth scale, which has not been previously achieved.

Conclusions

^{4}He, ^{20}Ne, ^{22}Ne, ^{36}Ar, and ^{40}Ar co-implanted ilmenite and olivine standards were prepared herein. We optimized the analytical conditions of the LIMAS for the multi-isotope depth profiling of ^{4}He, ^{20}Ne, ^{22}Ne, ^{36}Ar, ^{40}Ar, and major elements of ilmenite and olivine. All target ions except for ^{40}Ar were separated from the interference ions and determined using the ion assignment procedures for ilmenite and olivine standards.

The depth profiles of ^{4}He, ^{20}Ne, ^{22}Ne, ^{36}Ar, and ^{40}Ar were obtained by sputtering an area of $\sim 6 \times 8\ \mu m^2$, and the detection limits for ^{4}He, ^{20}Ne, ^{22}Ne, ^{36}Ar, and ^{40}Ar were respectively 7×10^{16}, 3×10^{16}, 9×10^{15}, 2×10^{16}, and 5×10^{16} cm^{-3} for ilmenite and 2×10^{17}, 4×10^{16}, 2×10^{16}, 2×10^{16}, and 9×10^{17} cm^{-3} for olivine. We evaluated the reproducibility of RSFs to calculate the noble gas compositions and concentrations. The reproducibility of the RSFs between independent measurement runs was in the 5–31% range (1SD). The stability of the $^{20}Ne/^{22}Ne$ ratios during depth profiling was restricted by counting errors. Therefore, this analytical method can be used to analyze solar wind noble gases in extraterrestrial materials. Based on the depth profiling of noble gases, this approach can reveal past solar activity and the underlying mechanisms of solar wind implantation and degassing processes.

Data availability

The data supporting this article have been included as part of the ESI.†

Author contributions

Y. O., K. B., and H. Y. designed the study. Y. O., K. B., and T. O. carried out the LIMAS analysis. All authors have approved the final version of the manuscript.

Conflicts of interest

There are no conflicts to declare.

Acknowledgements

We thank Dr Go Kinoda and Shingo Ogawa of the TORAY Research Center, Inc. for preparing the ion-implanted samples. We sincerely thank the two anonymous reviewers for their valuable comments, which have helped improve our manuscript. We acknowledge editorial handling by Dr Derya Kara Fisher. We also thank Charlesworth Author Services for their professional English editing services. This work was supported by grants from the Japan Society for the Promotion of Science (JSPS) KAKENHI and the Japan Science and Technology Agency (JST) to YO, KB, and HY.

References

1 R. Wieler, Do lunar and meteoritic archives record temporal variations in the composition of solar wind noble gases and nitrogen? A reassessment in the light of Genesis data, *Geochemistry*, 2016, **76**, 463–480.
2 C. M. Pieters and S. K. Noble, Space weathering on airless bodies, *J. Geophys. Res.:Planets*, 2016, **121**, 1865–1884.
3 T. Kirsten, Rare gages implanted in lunar fines, *Philos. Trans. R. Soc., A*, 1977, **285**, 391–395.
4 J. Kerridge, A reevaluation of the solar-wind sputtering rate on the lunar surface, *Lunar and Planetary Science Conference Proceedings*, 1991, vol. 21, pp. 301–306.
5 J. Kiko, H. W. Müller, K. Büchler, S. Kalbitzer, T. Kirsten and M. Warhaut, The gas ion probe: a novel instrument for analyzing concentration proeiles of gases in solids, *Int. J. Mass Spectrom. Ion Phys.*, 1979, **29**, 87–100.
6 J. Kiko, K. Büchler, J. Jordan, S. Kalbitzer, T. Kirsten, H. W. Müller, T. Plieninger and M. Warhaut, A comparison of rare gas concentration profiles in lunar and artificially

implanted ilmenites measured with the gas ion probe, *Meteoritics*, 1976, **11**, 309–311.
7 M. Warhaut, J. Kiko and T. Kirsten, Microdistribution patterns of implanted rare gases in a large number of individual lunar soil particles, *Lunar and Planetary Science Conference Proceedings*, 1979, vol. 10, pp. 1531–1546.
8 H. W. Müller, J. Kiko and T. Kirsten, He-depth profiles with high resolution (~100 Å) by the rare gas ion probe technique, *Meteoritics*, 1975, **10**, 459.
9 M. A. Ray, J. E. Baker, C. M. Loxton and J. E. Greene, Quantitative analysis and depth profiling of rare gases in solids by secondary-ion mass spectrometry: detection of $(CsR)^+$ molecular ions (R = rare gas), *J. Vac. Sci. Technol., A*, 1988, **6**, 44–50.
10 H. Yamazaki, Quantitative depth profiling of argon in tungsten films by secondary ion mass spectrometry, *Anal. Sci.*, 2001, **17**, 407–410.
11 A. Grimberg, H. Baur, P. Bochsler, F. Bühler, D. S. Burnett, C. C. Hays, V. S. Heber, A. J. G. Jurewicz and R. Wieler, Solar wind neon from Genesis: implications for the lunar noble gas record, *Science*, 2006, **314**, 1133–1135.
12 J.-P. Benkert, H. Baur, P. Signer and R. Wieler, He, Ne, and Ar from the solar wind and solar energetic particles in lunar ilmenites and pyroxenes, *J. Geophys. Res.*, 1993, **98**, 13147.
13 S. Ebata, M. Ishihara, K. Uchino, S. Itose, M. Matsuya, M. Kudo, K. Bajo and H. Yurimoto, Development of laser ionization mass nanoscope (LIMAS), *Surf. Interface Anal.*, 2012, **44**, 635–640.
14 K. Bajo, N. Kawasaki, I. Sakaguchi, T. T. Suzuki, S. Itose, M. Matsuya, M. Ishihara, K. Uchino and H. Yurimoto, *Anal. Chem.*, 2024, **96**, 5143–5149.
15 K. Bajo and H. Yurimoto, Nanoscale analysis of noble gas in solids, *J. Anal. Sci. Technol.*, 2024, **15**, 1–9.
16 K. Bajo, O. Fujioka, S. Itose, M. Ishihara, K. Uchino and H. Yurimoto, Electronic data acquisition and operational control system for time-of-flight sputtered neutral mass spectrometer, *Surf. Interface Anal.*, 2019, **51**, 35–39.
17 K. Bajo, S. Itose, M. Matsuya, M. Ishihara, K. Uchino, M. Kudo, I. Sakaguchi and H. Yurimoto, High spatial resolution imaging of helium isotope by TOF-SNMS, *Surf. Interface Anal.*, 2016, **48**, 1190–1193.
18 K. Bajo, C. T. Olinger, A. J. G. Jurewicz, D. S. Burnett, I. Sakaguchi, T. Suzuki, S. Itose, M. Ishihara, K. Uchino, R. Wieler and H. Yurimoto, Depth profiling analysis of solar wind helium collected in diamond-like carbon film from Genesis, *Geochem. J.*, 2015, **49**, 559–566.
19 K. Nagata, K. Bajo, S. Itose, M. Matsuya, M. Ishihara, K. Uchino and H. Yurimoto, Aberration-corrected focused ion beam for time-of-flight secondary neutral mass spectrometry, *Appl. Phys. Express*, 2019, **12**, 085005.
20 A. Tonotani, K. Bajo, S. Itose, M. Ishihara, K. Uchino and H. Yurimoto, Evaluation of multi-turn time-of-flight mass spectrum of laser ionization mass nanoscope, *Surf. Interface Anal.*, 2016, **48**, 1122–1126.
21 H. Yurimoto, K. Bajo, I. Sakaguchi, T. T. Suzuki, A. J. G. Jurewicz, S. Itose, K. Uchino and M. Ishihara, Quantitative analysis of helium by post-ionization method using femtosecond laser technique, *Surf. Interface Anal.*, 2016, **48**, 1181–1184.
22 D. S. Burnett, B. L. Barraclough, R. Bennett, M. Neugebauer, L. P. Oldham, C. N. Sasaki, D. Sevilla, N. Smith, E. Stansbery, D. Sweetnam and R. C. Wiens, The Genesis Discovery Mission: Return of Solar Matter to Earth, in *The Genesis Mission*, 2003, pp. 1–26.
23 J. F. Ziegler, M. D. Ziegler and J. P. Biersack, SRIM – The stopping and range of ions in matter, *Nucl. Instrum. Methods Phys. Res., Sect. B*, 2010, **268**, 1818–1823.
24 D. B. Reisenfeld, R. C. Wiens, B. L. Barraclough, J. T. Steinberg, M. Neugebauer, J. Raines and T. H. Zurbuchen, Solar Wind Conditions and Composition During the Genesis Mission as Measured by *in situ* Spacecraft, *Space Sci. Rev.*, 2013, **175**, 125–164.
25 P. Signer, H. Baur, U. Derksen, P. Etique, H. Funk, P. Horn and R. Wieler, Helium, neon, and argon records of lunar soil evolution, *Lunar and Planetary Science Conference Proceedings*, 1977, vol. 3, pp. 3657–3683.
26 K. Nagao, R. Okazaki, T. Nakamura, Y. N. Miura, T. Osawa, K. Bajo, S. Matsuda, M. Ebihara, T. R. Ireland, F. Kitajima, H. Naraoka, T. Noguchi, A. Tsuchiyama, H. Yurimoto, M. E. Zolensky, M. Uesugi, K. Shirai, M. Abe, T. Yada, Y. Ishibashi, A. Fujimura, T. Mukai, M. Ueno, T. Okada, M. Yoshikawa and J. Kawaguchi, Irradiation history of Itokawa regolith material deduced from noble gases in the Hayabusa samples, *Science*, 2011, **333**, 1128–1131.
27 D. Okumura, M. Toyoda, M. Ishihara and I. Katakuse, A compact sector-type multi-turn time-of-flight mass spectrometer 'MULTUM II', *Nucl. Instrum. Methods Phys. Res., Sect. A*, 2004, **519**, 331–337.
28 R. H. Nichols, C. M. Hohenberg and C. T. Olinger, Implanted solar helium, neon, and argon in individual lunar ilmenite grains: surface effects and a temporal variation in the solar wind composition, *Geochim. Cosmochim. Acta*, 1994, **58**, 1031–1042.